Accepted Manuscript

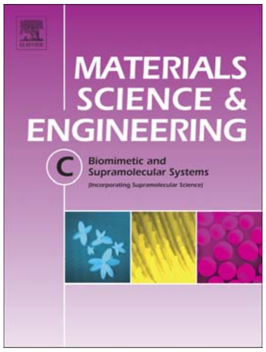

Effect of anodization on the surface characteristics and electrochemical behaviour of zirconium in artificial saliva

Daniela E. Romonti, Andrea V. Gomez Sanchez, Ingrid Milošev, Ioana Demetrescu, Silvia Cere

PII: S0928-4931(16)30079-0
DOI: doi: 10.1016/j.msec.2016.01.079
Reference: MSC 6170

To appear in: *Materials Science & Engineering C*

Received date: 17 September 2015
Revised date: 11 January 2016
Accepted date: 27 January 2016

Please cite this article as: Daniela E. Romonti, Andrea V. Gomez Sanchez, Ingrid Milošev, Ioana Demetrescu, Silvia Cere, Effect of anodization on the surface characteristics and electrochemical behaviour of zirconium in artificial saliva, *Materials Science & Engineering C* (2016), doi: 10.1016/j.msec.2016.01.079

Effect of anodization on the surface characteristics and electrochemical behaviour of zirconium in artificial saliva

Daniela E. Romonti[a], Andrea V. Gomez Sanchez[b], Ingrid Milošev[c], Ioana Demetrescu[a], Silvia Cere[b]

[a]*Faculty of Applied Chemistry and Materials Science, Department of General Chemistry, 1-7 Polizu, district 1, Bucharest Ro-011061, Romania*

[b]*INTEMA- Conicet- Universidad Nacional de Mar del Plata, Juan B. Justo, 4302 B7608FDQ, Mar del Plata, Argentina*

[c]*Jožef Stefan Institute, Department of Physical and Organic Chemistry, Jamova c. 39, SI-1000 Ljubljana, Slovenia*

Corresponding author

Dr. Silvia Cere

INTEMA, Universidad Nacional de Mar del Plata – CONICET

Juan B. Justo 4302, B7608FDQ

Mar del Plata, Argentina

Phone: +542234816600

Fax: +542234810046

e-mail: smcere@fi.mdp.edu.ar

Abstract

The paper is focused on elaboration of ZrO_2 films on pure zirconium via anodizing in phosphoric acid with and without fluoride at constant potentials of 30 V and 60 V. The structure and composition of the films were investigated using scanning electronic microscopy, Raman spectroscopy and X-ray photoelectron spectroscopy. The composition of the oxides formed at both potentials can be identified as monoclinic $ZrO_{2.}$ In addition to Zr and O, the layers formed in phosphoric acid contain phosphorus originating from the phosphoric acid. When the phosphoric acid solution contains NaF, fluorine is also incorporated into the oxide layer. The oxides formed at a higher voltage have greater roughness than those formed at 30 V. Anodized samples exhibit smaller current densities during anodic polarization compared to the as-received zirconium covered with *native* oxide.

Keywords: anodized zirconium, fluoride, XPS, corrosion resistance

Introduction

The surface characterization of materials employed in orthopaedic surgery is a topic of great importance because the surface plays a key role in the interaction between the metal and the host tissue. Surface modification induced by anodization under the conditions presented in this work corresponds to a surface design criterion based on the modification of the chemical and topological features in the micrometric range with the aim of promoting the osseointegration of the zirconium as a permanent implant.

Zirconium is, as a valve metal, very stable in numerous aggressive media and has been extensively used in the nuclear industry owing to its low neutron absorption and in the microelectronic industry [1,2] due to its high dielectric constant. More recently, Zr was investigated for biomedical applications [3-5]. It is biocompatible and has a lower ion release than Ti in bioenvironments due to its native passive oxide, which acts as a protective layer, according to the results obtained in Hanks' physiological solution [6]. Despite the fact that self-passivation is an easy and practical solution for biomaterials used for permanent implants, it does not provide any possibility for the further functionalization of the surface. Modifying the surface via anodization in phosphoric acid media seems to be a convenient way to stimulate bone formation [7]. Furthermore, it was reported that Zr-containing Ti alloys are nontoxic, non-allergenic and have good mechanical properties, even more suitable for bioapplications than TiAlV [8-12]. In line with this approach, new ternary and binary alloys with titanium have been investigated (TiAlZr and TiZr with various Zr contents), elaborating a large variety of micro and nanostructured TiO_2 and ZrO_2 oxides at voltages between 15 and 45 V in hybrid electrolytes [9-12]. Zirconium and titanium oxides can be tailored by controlling the anodization conditions, having structures from porous amorphous to crystalline layers. Their stability in bioenvironments and antibacterial properties can be correlated with their structure, denoting the relation between structure, properties and applications [13]. In a recent work, an atomic force microscopy (AFM) study of ZrO_2 fabricated in 0.1 mol/L ammonium oxalate at potentials between 0 V and 79 V showed a continuous decrease in roughness with the decreasing anodic potential [14].

In this manuscript, the electrochemical *in vitro* response of anodized zirconium was systematically studied to produce different surface topographies and to determine the effect of the surface modification process on the corrosion resistance of this metal. Although there have been many papers published about Ti and its alloys and Zr as an alloying element, the available literature on pure Zr is scarce, and, according to our knowledge, no reports in Afnor artificial saliva can be found [5-7, 11,12,15 -17]. This study presents the development of Zr oxides by anodization in phosphoric acid with and without the addition of fluoride ions for potential dental applications. F^- ions are known as strong modifiers of the structure of anodic oxides that may lead to structures from nanopores and nanotubes to microporosity depending on the anodic conditions [13,18, 19].

2. Experimental

2.1. Sample preparation and anodizing process

Flat samples of zirconium of 99.8% purity (Alfa Aesar) were cut into dimensions of 20 mm × 15 mm × 0.127 mm. The electrodes were anodized for 60 minutes in either 1 mol/L H_3PO_4 or a mixture of 1 mol/L H_3PO_4 and 0.15% w/v NaF using an electrophoresis power supply (Consort EV 231, Belgium). Before the anodization process, all of the samples were wet polished with 600 grit SiC paper, cleaned in ethylic alcohol for 10 minutes, washed with deionized water and dried at room temperature. Anodization was carried out in a two-electrode cell with the zirconium sample as the working electrode and a stainless steel mesh as the counter electrode, as described elsewhere [4].

The anodized samples were denoted as shown in Table 1.

2.2. Characterization of anodized samples

Surface characterization

The morphology and chemical composition of the oxide layers were studied by means of a scanning electron microscope (SEM, Quanta Inspect f, USA) equipped with an electron gun with field emission (FEG, field emission gun) and an energy dispersive X-ray spectrometer (EDS) with a resolution of 133 eV at Mn K.

X-ray photoelectron spectroscopy (XPS) was performed with a TFA Physical Electronics, Inc. spectrometer using non- and mono-chromatised Al K_{α} radiation (1486.6 eV) and a hemispherical analyser. The mono-chromatised radiation used for the high-resolution spectra yields a resolution of 0.6 eV, as measured on an Ag $3d_{5/2}$ peak. These spectra were used to differentiate between various species, while those obtained using non-monochromatized radiation were used to quantify the chemical composition. The take-off angle used, defined as the angle of emission relative to the surface, was 45º. The energy resolution was 0.5 eV. Survey scan spectra were recorded at a pass energy of 187.9 eV, and individual high-resolution spectra at a pass energy of 23.5 eV with an energy step of 0.1 eV. The diameter of the analysed spot was 400 μm. The values of the binding energies were aligned to the carbon peak C 1 s at 284.8 eV. After taking the surface spectra, the depth profiling of the oxidized layers was performed. An Ar^+ ion beam, with an energy level of 3 keV and a raster of 3 mm × 3 mm (sputter rate 0.67 nm/min determined on a Ni/Cr multilayer standard), was used for sputtering.

The crystalline domains present in the anodic oxides were determined by Raman spectroscopy using an Invia Reflex confocal Raman microscope (Renishaw, UK). The Raman spectra were obtained using a 514 nm argon laser with a 50× objective lens. No thermal effects were observed on the samples during these measurements.

The topography of the anodized samples was analysed using an A100-SGS atomic force microscope (AFM) (A.P.E. Research Italy). AFM measurements were performed in contact mode. The calculated roughness values are basically the arithmetic average of the absolute values of the highest and lowest points of the samples, also taking in consideration the slopes of the surface (so it does not necessarily mean that the sample with the greatest height also has the highest roughness value). Roughness values were calculated after creating a baseline and levelling the image with the minimum amount of image preparation, as data may be lost during the processing.

Electrochemical characterization

After the anodizing process, the samples were electrochemically tested in Afnor artificial saliva (Table 2) [20]. All reagents were supplied by Sigma-Aldrich (analytical grade). Deionized water (18.2 MΩ cm, Millipore) was used throughout. Electrochemical tests were performed using a conventional three-electrode cell with a saturated calomel electrode (SCE, Radiometer Analytical, France) as reference and a platinum wire as counter electrode. Before each measurement, the potential was left to stabilize for 40 minutes at open circuit. Potentiodynamic polarization curves were measured from the open circuit potential to 1.0 V and backwards at a sweep rate of 0.002 V/s. Electrochemical impedance spectroscopy (EIS) measurements were carried out with an amplitude of the perturbation signal of 10 mV rms, and the impedance was measured between 10^{-2} and 10^{6} Hz. The impedance data were fitted to equivalent circuit models with Zplot for Windows software [21]. Electrochemical measurements were taken at 37 ºC using a Vicking 4100 (Vicking Argentine) thermostatic bath.

3. Results and discussion

3.1 Anodization process

After the anodization process, the zirconium samples acquired different colours (Fig. 1). The obtained colours include the same shades as in previously reported data [4].

3.2. Surface characterization: Morphology and elemental analysis

The morphology and the chemical composition of the samples were studied by SEM/EDS analysis. SEM images of anodized zirconium samples recorded at different magnifications are presented in Figure 2.

The oxide layers formed for samples 60P and 30 P present discontinuities distributed on the surface. Porosity is also observed for the 30 PF and 60PF samples, together with a smoother surface. Although some authors found a nanotubular structure in anodic films formed in F-containing [18] aqueous electrolyte solutions, nanotubes were not observed herein in samples formed in phosphoric acid containing fluoride. Because the electrolyte concentration, anodization potential and time under potentiostatic control and even stirring regimen are known to be critical parameters for the anodic film structure, the anodic film growth parameters used in this work may not be adequate for nanotube formation. Further, more detailed studies of anodizing parameters may be performed to evaluate the capability of NaF additions to phosphoric acid to obtain ordered oxide structures in the nanoscale.

The topography of the anodized zirconium samples was evaluated using atomic force microscopy. AFM images are presented in Figure 3, and the values of the surface roughness (R_a) for the samples are presented in Table 3. Samples anodized at 30 V either with phosphoric acid or with phosphoric acid + sodium fluoride present less roughness than those anodized at 60 V. These results reflect changes in the topography of the zirconium surface with anodization at different potentials, in agreement with previous reports by Cox for anodised Zr and Zircaloy-2 in various electrolytic media [22]. The different types of surface roughness have been extensively discussed by Löberg et al., [23], along with its relation with the osseointegration properties of dental implants. Animal studies have shown that the interfacial shear strength of bone-anchored implants can be increased by providing the implant with a rough surface [24-25]. EDS measurements confirm the presence of zirconium and oxygen in all anodized samples (Figure 4). Samples anodized in the mixture of phosphoric acid and sodium fluoride also contain sodium and fluorine coming from the electrolyte. It has been reported that fluoride ions enhance the incorporation of newly formed collagen into the bone matrix, increase the rate of the formation of apatite on the surface and the pull out and removal torque forces, and improve the thrombogenic properties and osteoblast differentiation [27].

Raman spectra obtained for zirconium oxides anodized under different conditions compared with as-received zirconium are presented in Figure 5. The spectra of all of the anodized samples present the same peak position, relative intensity and peak shape While in as-received pure zirconium, tetragonal ZrO_2 was evidenced by the presence of the main peak of this crystallographic phase (263 cm^{-1}), in the anodized films, no evidence of tetragonal zirconium was found. Anodic film growth at different potentials and even in different acid electrolytes presents peaks at 177.4, 216.6, 334.1, 378.8, 476.8, 560.6, 624.8, and 756.3 cm^{-1}. All of these peaks correspond to monoclinic ZrO_2. [28-30]. The incorporation of species from the anodizing electrolyte into the anodic films may be one reason for the broad peaks of the Raman spectra, as was previously discussed by Ismail et al. [18].

The chemical composition of the anodized zirconium samples was further analysed using X-ray photoelectron spectroscopy which, in addition to the general composition, offers information on the chemical speciation as well. The layer formed by anodization comprises mainly zirconium oxide (Table 4). Carbon is present only as adventitious carbon. In addition to Zr and O, the layers formed in phosphoric acid contain phosphorus originating from the phosphoric acid. N and Na are present as contaminants from solution. When the phosphoric acid contains NaF, fluorine is incorporated into the oxide layer at concentrations greater than that of P.

The chemical composition of the layers formed by anodization was further studied by high-resolution spectra to identify the oxidation state of the individual elements and their chemical environment (Figs. 6 and 7). The centre of the XPS $3d_{5/2}$ peak of zirconium metal was reported at 178.3-179.3 eV and that of ZrO_2 at 181.5-184.0 eV [31,32]. The centre of the XPS $3d_{5/2}$ peak of anodized zirconium at 182.3-182.6 eV confirms that the surface is completely oxidized and the peak related to zirconium metal is not present (Fig. 6a). No significant change in peak shape or position is observed among the different anodized zirconium samples, indicating that ZrO_2 is the major oxidation product under all conditions studied. The position of the centre of the O 1 s peak depends on the hydration of the layer: oxide component, O^{2-}, at 530.1–530.3 eV, hydroxide component, OH^- at 531.4–531.6 eV, and water, H_2O, and/or phosphate containing species, PO_4^{3-}, at 532.3-532.5 eV [32-34]. The position of the peak centre at higher binding energy, 531.5 eV, for samples anodized in phosphoric acid only (Fig. 6b) is consistent with the larger concentration of phosphorus in the layer (Table 4). For the samples oxidized in the solution containing NaF, the peak centres at 530.2 and 530.9 eV are located in oxide (O^{2-}) range. This shift to lower binding energy in the presence of fluorine can be ascribed to the presence of fluorine in the oxide layer. Mixed oxides SiO_2-ZrO_2 prepared by the hydrolysis of H_2SiF_6 and H_2ZrF_6 that contain residual fluorine show a shift in the position of the O 1 s peak as the concentration of fluorine in the oxide increases [31]. Whilst in the ZrO_2, the peak centre was at 532.4 eV, it was at 530.4 eV in the presence of fluorine [35]. This shift agrees with the data presented herein.

The centre of the XPS 2p phosphorus peak appears at 133.2 eV (Fig. 7a). The P 2p spectrum should theoretically be a non-resolved doublet with $2p_{1/2}$ and $2p_{3/2}$ components with a difference in binding energy of 0.8 eV and area ratio of 1:2. The position of the peak centre indicates that phosphorus is present as phosphate [31-33]. Zirconium anodized in phosphoric acid containing NaF contains fluorine (Table 4). The centre of the F 1 s peak is located at 685.2 eV (60PF) and 685.5 eV (30PF) (Fig. 7b). The position of this peak correlates with that of zirconium(IV) tetrafluoride ZrF_4 (685.1 and 685.9 eV) or ZrO_2 containing fluorine (685.3 eV for the ZrO_2 containing 10.5 at.% F) [33]. The peak related to NaF occurs at a lower binding energy (684.3 eV) [28].

To investigate the in-depth composition of the layers, XPS depth profiles were measured for the 60P and 60PF samples (Fig. 8). From previous work, it is known that the layer thickness is above 100 nm [30], so that only the upper part of the layer was analysed (~10 nm). The content of carbon for both samples decreased within the first two minutes of sputtering, indicating that it is present mainly at the sample surface as adventitious carbon. After approximately 2 minutes (~1.3 nm), the carbon content dropped, and the composition of the bulk layers is attained. As the sputter process proceeds the zirconium oxide is stable, in accordance with its much larger thickness. For the sample 60P, the concentration of phosphorus decreased from 5.7 at.% to 2 at.% after only two minutes and then remained constant. This indicates that P is enriched at the layer surface, as was previously suggested [30]. For the samples 60PF, the concentration of P is very small. Instead, fluorine appeared. Its concentration peaked just below the surface and then remained stable in the layer depth at ~8 at.%. A concomitant decrease in O concentration occurs when compared to sample 60P. These results prove that with the presence of fluoride in the phosphoric acid bath, zirconium oxide fluoride is formed, which contains residual phosphate. In contrast, anodization in phosphoric acid results in the formation of ZrO_2, which contains up to 6 at.% phosphate, which is enriched at the top of the layer.

3.3 Electrochemical behaviour in artificial saliva

Anodic polarization curves recorded in artificial saliva (Afnor) solution of as-received and anodized zirconium at different potentials in acid solutions are shown in Figure 9. The anodized samples exhibit lower current densities during the anodic polarization compared to the as-received zirconium covered with *native* oxide.

The anodic oxides grown in the acid solutions, with or without fluoride, act as a barrier against the dissolution of the underlying zirconium in Afnor solution. The polarization curves for the anodized samples assume a similar shape to those of the as-received substrate, yet the current density is reduced. At potentials more positive than 0 V, a passive range can be determined. It extends for at least 0.4 V (depending on the sample under study, see Fig. 9) followed by an abrupt current density increase due to the localized breakdown of the passive film. Once localized corrosion starts, the oxide repassivation in Afnor is not possible, as indicated by the continuous current density increase and the appearance of hysteresis in the reversal sweep. The breakdown of the passive film during anodic polarization was observed for all anodized samples and for the as-received zirconium. The 60PF sample presents the lower current densities around the corrosion potential; however, it is subjected to passive breakdown at a more negative potential compared to other samples. Similar behaviour is observed for the 30PF sample, whereas the 30P and 60P samples exhibited more positive values of the breakdown potential. This is probably due to the difference in the chemical composition on the surface (as shown in XPS). Electrochemical parameters are shown in Table 5.

EIS diagrams in the form of Nyquist and Bode plots are presented in Figure 10 for the four conditions under study after 40 min of immersion in Afnor solution and compared to the as-received zirconium sample. To obtain a better insight into the system response, the EIS data were fitted by means of an electrical equivalent circuit, relating the high-frequency component of the Bode plot to the electrical properties of the film present on the surface [36].

For all samples, the slope of the impedance modulus *vs* frequency plot differs from unity and can be assumed as a non-ideal capacitor. This behaviour is characteristic of passive films and has been observed for oxide films of valve metals [5,37-39]. For the analysis of the EIS results, a constant phase element impedance contribution (Z_{CPE}) was used [40], accounting for the deviations in the modulus Bode plot. Z_{CPE} is given by

$$Z_{CPE} = 1/Q(j\omega)^{\alpha} \qquad (1)$$

where Q is a parameter independent of frequency and α is a coefficient associated with the system homogeneity [41,42]. The origin of a CPE response is related to the distribution of time constants, but a great variety of explanations are reported in the literature [43,44].

For a parallel distribution of time constants at the electrode surface, Brug et al. [45] described the effective capacitance (C_{eff}) associated with the *CPE* element as

$$C_{eff} = Q^{1/\alpha}(R_e^{-1}+R_{ox}^{-1})^{(1-\alpha)/\alpha} \qquad (2)$$

where R_e is the electrolyte ohmic resistance, R_{ox} relates to the charge transfer resistance associated with the kinetics of oxide growth and Q and α have the same meaning as in Equation (1).

The experimental data were fitted with the electrical equivalent circuit shown in Figure 11. This circuit has been broadly used in the literature to represent porous oxides and also the bilayer structure of many passive films [30], where the interior circuit represents the inner layer. The results obtained by data fitting and by applying eq. 3 are presented in Figure 12.

All anodized samples present similar values of C_{eff} that are much lower than that of the as-received Zr. This indicates a better capacitive effect of the oxide layers formed under anodized conditions and, assuming a similar dielectric constant for the developed oxides, an increased film thickness. Conversely, R_{ox} for all of the coated samples is increased by an order of magnitude compared to the as-received substrate. Therefore, all anodized samples present better corrosion resistance in artificial saliva. When comparing the surface treatments, the 60PF sample exhibits a larger R_{ox} and smaller C_{eff}, suggesting a more compact and isolating film. R_{ox} values can be related to a decrease of the pore area, offering a higher resistance to electron transfer in the base of the pores. The other two samples, 30P and 30PF, show similar behaviour, which is intermediate compared to that of samples 60P with the lowest R_{ox} (Figs. 12 a and b). It is worth noting, however, that although all of the anodized conditions present similar parameters after immersion in Afnor, the samples without the fluoride treatment present a more positive breakdown potential than those with fluoride, giving a wider range of passivity for the former samples. The influence of fluoride ions in the oxide formation and stability is complex, and it has been reported that the ZrO_2 nanotube formation in F^--containing electrolytes is the result of the competition between the electrochemical oxide formation and the chemical dissolution of said oxide by fluoride ions, as shown in the equation below [46, 47].

$$Zr + 2\,H_2O \rightarrow ZrO_2 + 4\,H^+ + 4\,e^- \qquad (3)$$

$$ZrO_2 + 4\,H^+ + 6\,F^- \rightarrow [ZrF_6]^{2-} + 2\,H_2O \qquad (4)$$

The increase in the anodizing voltage from 20 to 80 V transforms the ordered nanotubular structures on titanium to a porous distributed surface with a significant variation in roughness [47]. The morphologies observed for the oxidized layers suggest that the pore formation may be driven by the localized dissolution of ZrO_2. The localized dissolution can reduce the thickness of the oxidized layer, increasing the electric field intensity at the bottom of the pore and inducing the formation of new oxide [46]. It is noteworthy that in the system containing fluoride, despite the fact that anodization was performed at the same voltage (60 V), the current density is smaller than for 60P. At 30 V in the system with fluoride, the corrosion rate is only half that of the one for the system without fluoride.

Conclusions

Experimental data (Raman spectra and X-ray photoelectron spectroscopy) demonstrate that monoclinic ZrO_2 is present on Zr after anodization in phosphoric acid with and without fluoride at various potentials. When the phosphoric acid contains NaF, fluorine is incorporated into the oxide layer. Anodized samples exhibit lower current densities during anodic polarization compared to the as-received zirconium covered with *native* oxide. All anodized samples present a breakdown of the passive film during anodic polarization in Afnor artificial saliva, being lower for the samples anodized in phosphoric acid with sodium fluoride. The incorporation of fluorine into the oxide layer as seen by XPS could induce some type of defective site that lowers the breakdown potential. However, the surface treatment achieved by anodizing Zr at 60 V in the mixture of phosphoric acid and NaF seems to be the most promising from the point of view of the corrosion behaviour. Further studies regarding the bioactivity of this alloy with the optimal surface treatment should be conducted.

Acknowledgments

The work has been funded by the Sectorial Operational Programme Human Resources Development 2007-2013 of the Ministry of European Funds through the Financial Agreement POSDRU/159/1.5/S/134398. The authors wish to thank the Romania-Argentine bilateral program 729/23.07.2013, RO12-03. The financial support by the Slovenian Research Agency is acknowledged (grant No. P3-0393). The authors thank Dr. J. Kovač from the Jožef Stefan Institute for XPS measurements and Dr M. Desimone from INTEMA for the Raman measurements.

References

[1] B. Cox, Some thoughts on the mechanisms of in-reactor corrosion of zirconium alloys, J. Nuc. Mat 336 (2005) 331–368.

[2] A. Javey, H. Kim, M. Brink, Q. Wang, A. Ural, J. Guo, P. McIntyre, P. McEuen, M. Lundstrom, H. Dai, High-κ dielectrics for advanced carbon-nanotube transistors and logic gates, Nat. Mater. 1 (2002) 241–246.

[3] Y.B. Wang, Y.F. Zheng, S.C. Wei, M. Li, In vitro study on Zr-based bulk metallic glasses as potential biomaterials, J. Biomed. Mater. Res. B Appl. Biomater. 96 (2011) 34–46.

[4] A. Gomez Sanchez, W. Schreiner, G. Duffo, S. Cere, Surface characterization of anodized zirconium for biomedical applications, Appl. Surf. Sci. 257 (2011) 6397–6405.

[5] A. Gomez Sanchez, J. Ballarre, J. C. Orellano, G. Duffó, S. Cere, Surface modification of zirconium by anodisation as material for permanent implants: in vitro and in vivo study, J. Mater. Sci. - Mater. Med., 24 (2013) 161–169.

[6] T. Hanawa, Y. Tsutsumi, Calcium Phosphate Formation on Titanium and Zirconium and Its Application to Medical Devices, Ashdin Publishing, Bioceramics Development and Applications 1 (2011) Article ID D110119, doi:10.4303/bda/D110119.

[7] M. R. Katunar, A. Gomez Sanchez, J. Ballarre, M. Baca, C. Vottola, J. C. Orellano, H. Schell, G. Duffo, S. Cere, Can anodised zirconium implants stimulate bone formation? Preliminary study in rat model, Prog. Biomater. 3 (2014) 1-10. DOI10.1007/s40204-014-0024-9.

[8] M. Mindroiu, E. Cicek, F. Miculescu, I. Demetrescu, The influence of thermal oxidation treatment on the electrochemical stability of TiAlV and TiAlFe alloys and their potential application as biomaterials, Rev. Chim. 58 (2007) 898–903.

[9] H. Tsuchiya, P. Schmuki, Thick self-organized porous zirconium oxide formed in H_2SO_4/ NH_4F electrolytes, Electrochem. Commun. 6 (2004) 1131–1134.

[10] H. Tsuchiya, J.M. Macak, L. Taveira, P. Schmuki, Fabrication and characterization of smooth high aspect ratio zirconia nanotubes, Chem. Phys. Lett. 410 (2005) 188–191.

[11] S. Grigorescu, A.B. Stoian, D. Ionita, I. Demetrescu, Corrosion behavior of anodized TiAlZr alloy in a hybrid electrolyte at different voltages, Mater. Corr. 65 (2014) 897–901.

[12] D. Ionita, M. Grecu, C. Ungureanu, I. Demetrescu, Modifying the TiAlZr biomaterial surface with coating for a better anticorrosive and antibacterial performance, Appl. Surf. Sci. 257 (2011) 9164–9168.

[13] S. Grigorescu, C. Ungureanu, R. Kirchgeorg, P. Schmuki, I. Demetrescu, Various sized nanotubes on TiZr for antibacterial surfaces, Appl. Surf. Sci. 270 (2013) 190–196.

[14] J. Padmaja, Ch. Anjaneyulu, Anodic oxide films of Zr-4 in 0.1M ammonium oxalate by AFM studies, Arch. Appl. Sci. Res. 5 (2013) 1–7.

[15] X. Ye, Y. Yang, G. Tang, Microhardness and corrosion behavior of surface gradient oxide coating on the titanium alloy strips under high energy electro-pulsing treatment, Surface and Coatings Technology 258 (2014) 467-484.

[16] X. Ye, Z.T.H. Tse, G. Tang, Y. Geng, G. Song, Influence of electropulsing globularization on the microstructure and mechanical properties of Ti–6Al–4V alloy strip with lamellar microstructure, Materials Science and Engineering: A 622 (2015) 1-6.

[17] X. Ye, Z.T.H. Tse, G. Tang, G. Song, Effect of electroplastic rolling on deformability, mechanical property and microstructure evolution of Ti–6Al–4V alloy strip, Materials Characterization 98 (2014) 147-161

[18] S. Ismail, Z.A. Ahmad, A. Berenov, Z. Lockman, Effect of applied voltage and fluoride ion content on the formation of zirconia nanotube arrays by anodic oxidation of zirconium, Corr Sci 53 (2011) 1156–1164.

[19] C.C. Manole, C. Pirvu, I. Demetrescu, TiO_2: from nanotubes to nanopores by changing the anodizing voltage in fluoride-glycerol electrolyte, Key Eng. Mater. 415 (2009) 5–8.

[20] D. Ionita, M. Prodana, I. Demetrescu, S. G. Stanciu, G. A. Stanciu, Electrochemical stability and surface analysis in evaluation fluoride effect on new bioalloy Ti7Al3V2Mo2Fe used in dentistry, Mater. Corros. 62 (2011) 1111–1116.

[21] Zplot for Windows, Electrochemistry, Impedance Software Operating Manual, Part 1, Scribner Ass. Inc., Southern Pines, NC 1998.

[22] B. Cox, Factors affecting the growth of porous anodic oxide films on zirconium, J. Electrochem. Soc. 117 (1970) 654–663.

[23] J. Löberg, I. Mattisson, S. Hansson, E. Ahlberg, Critical assessment of surface roughness parameters, Open Biomater. J. 2 (2010) 18–35.

[24] A. Wennerberg, T. Albrektsson, Effects of titanium surface topography on bone integration: a systematic review. Clin. Oral Impl. Res. 20 (2009) 172–184. doi: 10.1111/j.1600-0501.2009.01775.x

[25] C.-J. Ivanoff, C. Hallgren, G. Widmark, L. Sennerby, A. Wennerberg, Histologic evaluation of the bone integration of TiO_2 blasted and turned titanium microimplants in humans, Clin. Oral Impl. Res. 12 (2001) 128–134.

[26] H. Hahn, W. Palich, Preliminary Evaluation of Porous Metal Surfaced Titanium for Orthopedic Implants, J. Biomed. Mater. Res. 4 (1970) 571–577.

[27] I.U. Petersson, J.E.L. Löberg, A.S. Fredriksson, E.K. Ahlberg, Semi-conducting properties of titanium dioxide surfaces on titanium implants, Biomaterials 30 (2009) 4471–4479.

[28] J. E. Maslar, W. S. Hurst, W. J. Bowers Jr., J. H. Hendricks, In Situ Raman Spectroscopic Investigation of Stainless Steel Hydrothermal Corrosion, J. Nucl. Mat. 298 (2001) 239–247.

[29] L. Kumari, G.H. Du, W.Z. Li, R. S. Vennila, S. K. Saxena, D. Z. Wang, Synthesis, microstructure and optical characterization of zirconium oxide nanostructures, Ceram. Int. 35 (2009) 2401–2408.

[30] A. Gomez Sanchez, M. Katunar, W. Schreiner, G. Duffó, S. Ceré, D.J. Schiffrin, Structure and dielectric properties of electrochemically grown ZrO_2 films, Acta Chim. Slov. 61 (2014) 316–327.

[31] NIST X-ray Photoelectron Spectroscopy Database, NIST Standard Reference Database 20, Version 3.5, Data compiled and evaluated by C.D. Wagner, A.V. Naumkin, A. Kraut-Vass, J.W. Allison, C.J. Powell, J.R. Rumble, Jr., http://srdata.nist.gov/xps/

[32] I. Milošev, G. Žerjav, J. Calderon Moreno, M. Popa, Electrochemical properties, chemical composition and thickness of passive film formed on novel Ti-20Nb-10Zr-5Ta alloy, Electrochim. Acta, 99 (2013) 176–189.

[33] I. Milošev, M. Metikoš-Huković, Ž. Petrović, Influence of preparation methods on the properties of self-assembled films of ocytadecylphosphonate on Nitinol: XPS and EIS studies, Mater. Sci. Eng. C, 32 (2012) 2604–2616.

[34] I. Milošev, B. Kapun, V.S. Šelih, The effect of fluoride ions on the corrosion behaviour of Ti metal, and Ti-6Al-7Nb and Ti-6Al-4V alloys in artificial saliva, Acta Chim. Slov. 60 (2013) 543–555.

[35] H.J.M. Bosman, A.P. Pijpers, A.W.M.A. Jaspers, An X-ray photoelectron spectroscopy study of the acidity of SiO_2–ZrO_2 mixed oxides, J. Catal. 161 (1996) 551–559.

[36] A. Conde, J.J. de Damborena, Electrochemical impedance spectroscopy for studying the degradation of enamel coatings, Corr. Sci. 44 (2002) 1555–1567.

[37] W.A. Badawy, S.S. Elegamy, Kh.M. Ismail, Comparative study of tantalum and titanium passive films by electrochemical impedance spectroscopy, Br. Corros. J. 28 (1993) 133–136.

[38] O. Kerrec, D. Devilliers, H. Groul, M. Chemla, Dielectric properties of anodic oxide films on tantalum, Electrochim. Acta. 40 (1995) 719–724.

[39] M. J. Esplandiu, E. M. Patrito, V. A. Macagno, Characterization of hafnium anodic oxide films: An AC impedance investigation, Electrochim. Acta. 40 (1995) 809–815.

[40] J. Ross Macdonald, W. B. Johnson, Impedance Spectroscopy. Chapter one, John Wiley & Sons, New York, 1987.

[41] J.B. Jorcin, M.E. Orazem, N.P. Pébère, B. Tribollet, CPE analysis by local electrochemical impedance spectroscopy, Electrochim. Acta. 51 (2006) 1473–1479.

[42] M. Orazem, B. Tribollet, Electrochemical Impedance Spectroscopy (ECS), John Wiley & Sons, New York, 2008.

[43] C.H. Kim, S.I. Pyun, J.H. Kim, An investigation of the capacitance dispersion on the fractal carbon electrode with edge and basal orientations, Electrochim. Acta 48 (2003) 3455–3463.

[44] C.A. Schiller, W. Strunz, The evaluation of experimental dielectric data of barrier coatings by means of different models, Electrochim. Acta 46 (2001) 3619–3625.

[45] G.J. Brug, A.L.G. Van Den Eeden, M. Sluyters-Rehbach. J.H. Sluyters, The analysis of electrode impedances complicated by the presence of a constant phase element, J. Electroanal. Chem. 176 (1984) 275–295.

[46] L. Zhang, J. Shao, Y. Han, Enhanced anodization growth of self-organized ZrO2 nanotubes on nanostructured zirconium, Surf. Coat. Technol. 205 (2011) 2876–2881.

[47] J.M. Macak, H. Tsuchiya, A. Ghicov, K. Yasuda, R. Hahn, S. Bauer, P. Schmuki, Curr. Opin. Solid State Mater. Sci. 11 (2007) 3–18.

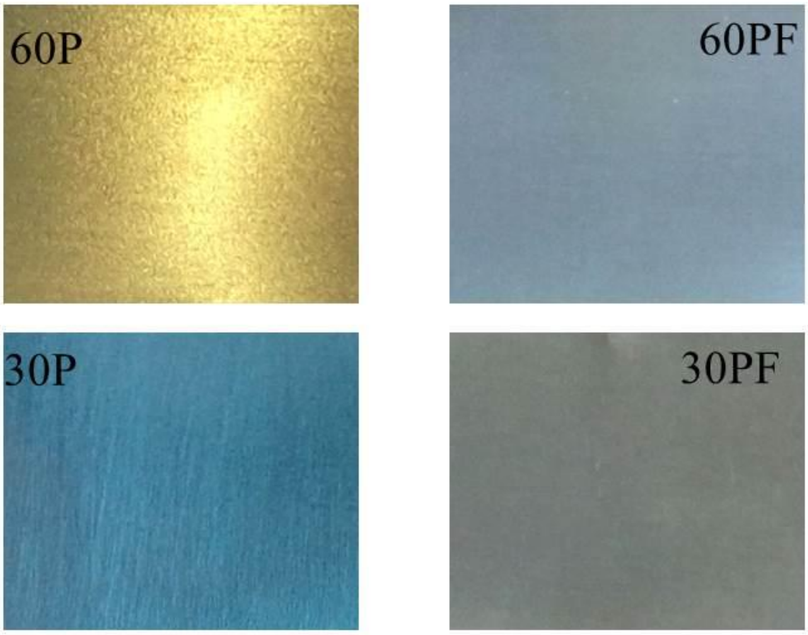

Figure 1

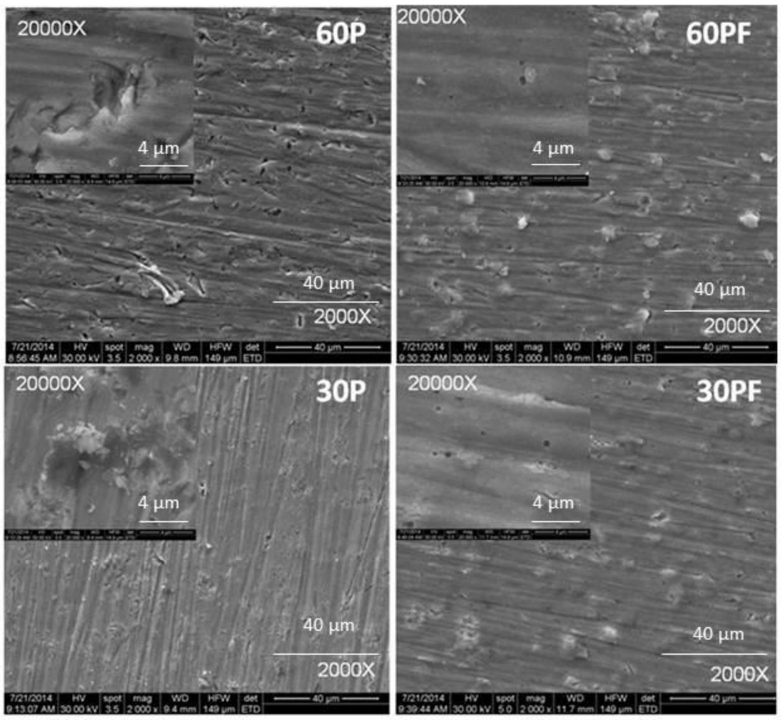
20000X
60P
4 µm
40 µm
2000X
20000X
60PF
4 µm
40 µm
2000X
20000X
30P
4 µm
40 µm
2000X
20000X
30PF
4 µm
40 µm
2000X

Figure 2

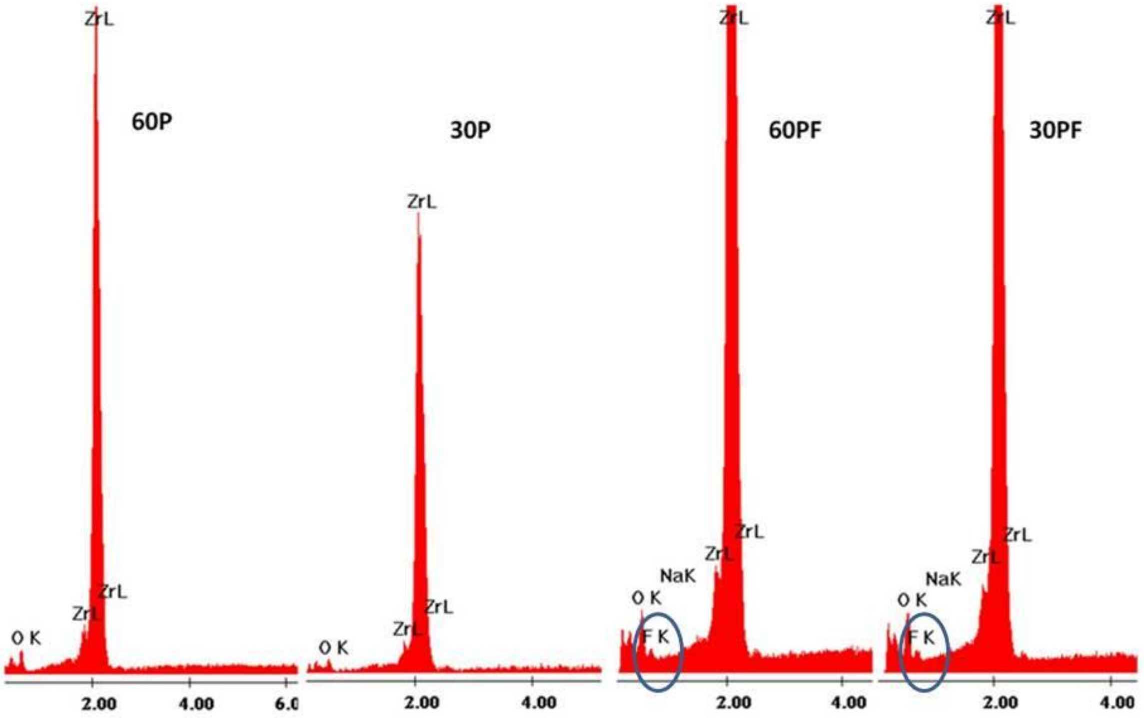
ZrL
60P
O K
ZrL
ZrL
2.00
4.00
6.0
30P
ZrL
O K
ZrL
ZrL
2.00
4.00
60PF
ZrL
NaK
O K
F K
ZrL
ZrL
2.00
4.00
30PF
ZrL
NaK
O K
F K
ZrL
ZrL
2.00
4.00

Figure 3

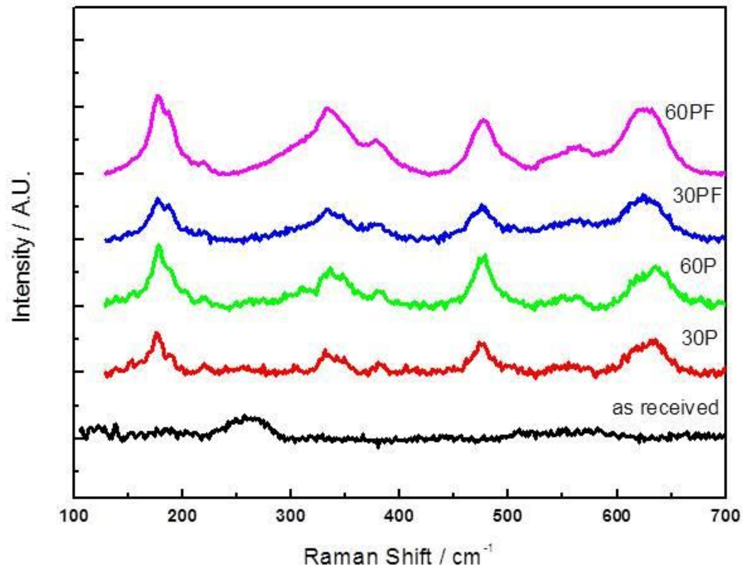
60PF
30PF
60P
30P
as received
Intensity / A.U.
100
200
300
400
500
600
700
Raman Shift / cm⁻¹

Figure 4

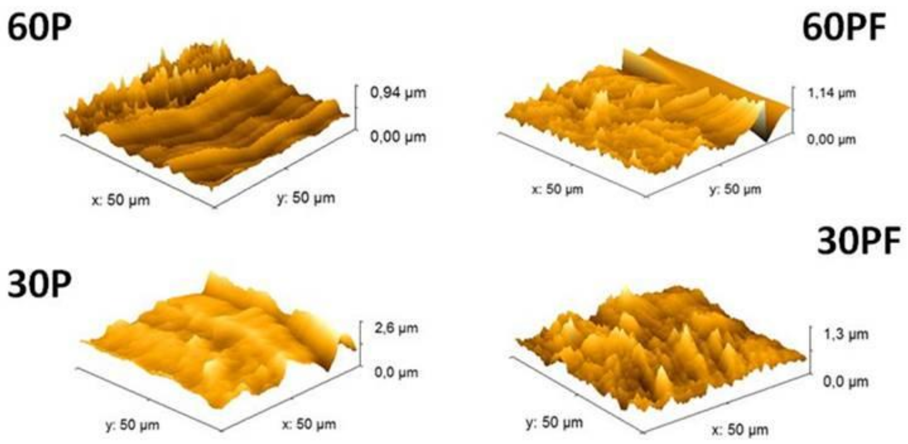

60P
0,94 µm
0,00 µm
x: 50 µm
y: 50 µm
60PF
1,14 µm
0,00 µm
x: 50 µm
y: 50 µm
30P
2,6 µm
0,0 µm
y: 50 µm
x: 50 µm
30PF
1,3 µm
0,0 µm
y: 50 µm
x: 50 µm

Figure 5

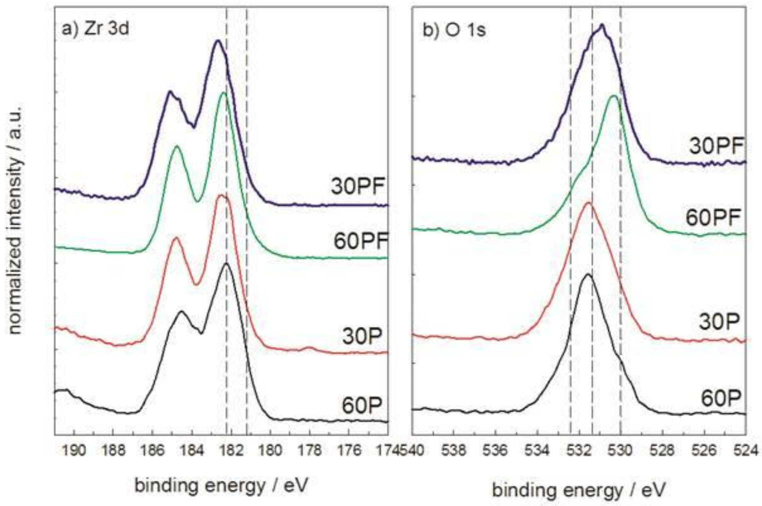
a) Zr 3d
b) O 1s
normalized intensity / a.u.
30PF
60PF
30P
60P
30PF
60PF
30P
60P
190
188
186
184
182
180
178
176
174
540
538
536
534
532
530
528
526
524
binding energy / eV
binding energy / eV

Figure 6

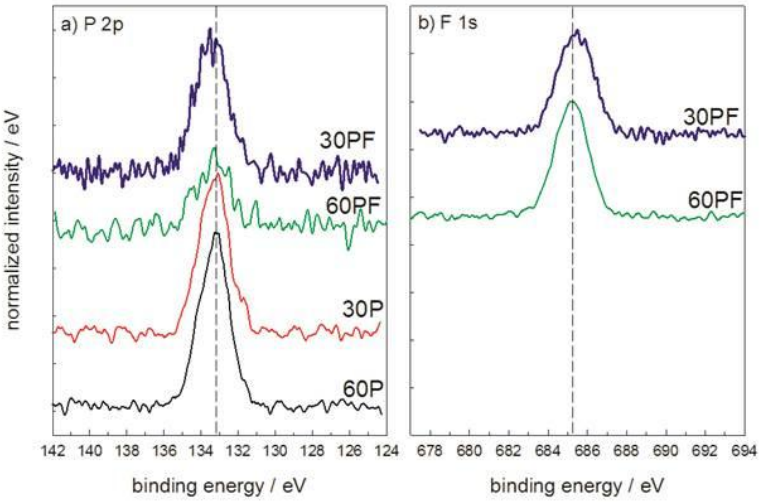
a) P 2p
b) F 1s
normalized intensity / eV
30PF
60PF
30P
60P
30PF
60PF
142 140 138 136 134 132 130 128 126 124
678 680 682 684 686 688 690 692 694
binding energy / eV
binding energy / eV

Figure 7

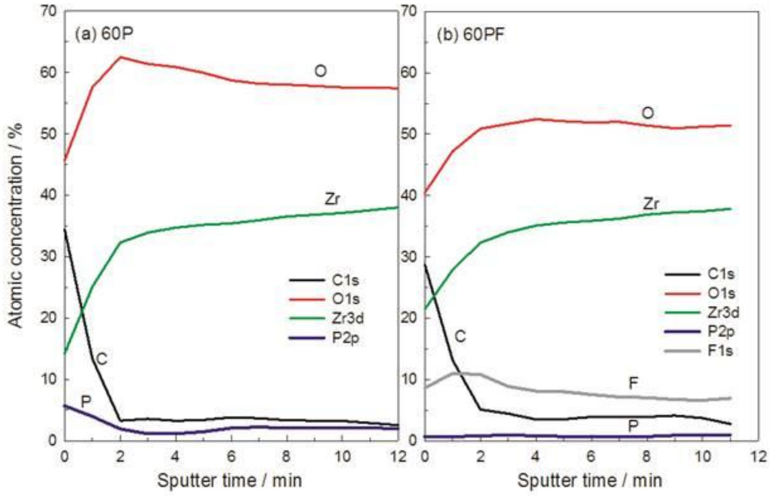

(a) 60P
(b) 60PF
Atomic concentration / %
Sputter time / min
Sputter time / min
O
Zr
C
P
F
C1s
O1s
Zr3d
P2p
F1s
0
10
20
30
40
50
60
70
0
2
4
6
8
10
12

Figure 8

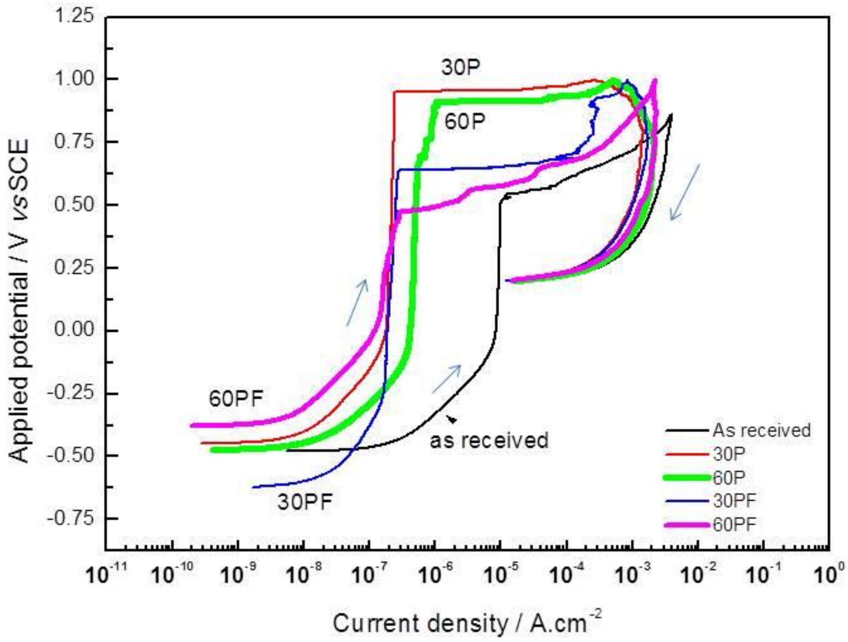

1.25
1.00
0.75
0.50
0.25
0.00
-0.25
-0.50
-0.75
Applied potential / V vs SCE
30P
60P
60PF
30PF
as received
As received
30P
60P
30PF
60PF
10^{-11} 10^{-10} 10^{-9} 10^{-8} 10^{-7} 10^{-6} 10^{-5} 10^{-4} 10^{-3} 10^{-2} 10^{-1} 10^{0}
Current density / $A.cm^{-2}$

Figure 9

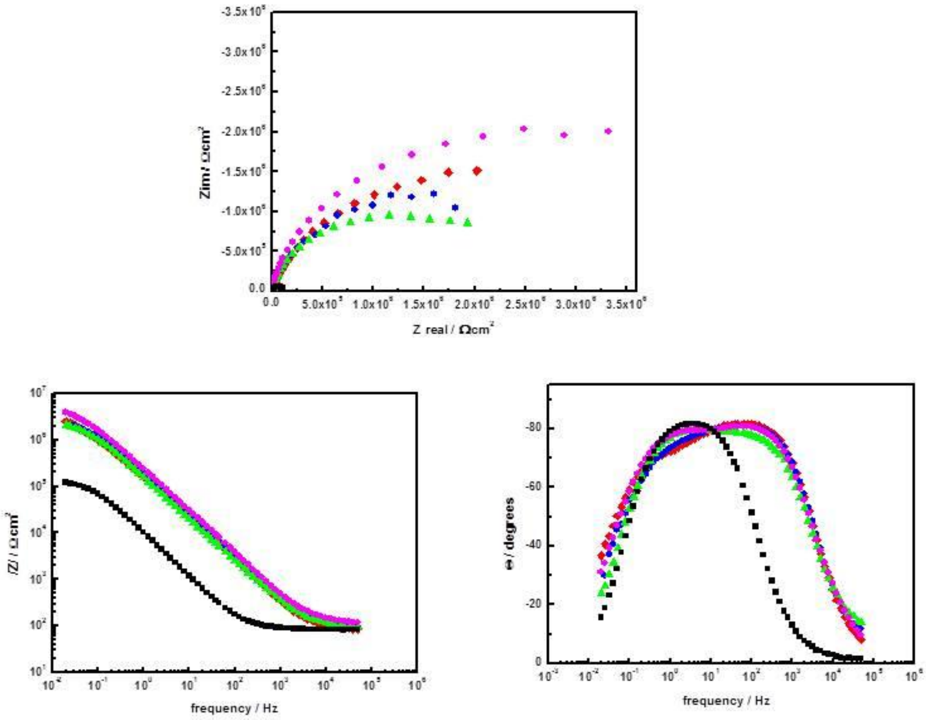

Zim / Ωcm²
Z real / Ωcm²
|Z| / Ωcm²
frequency / Hz
Θ / degrees
frequency / Hz

Figure 10

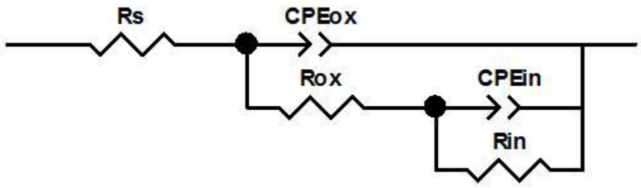

Figure 11

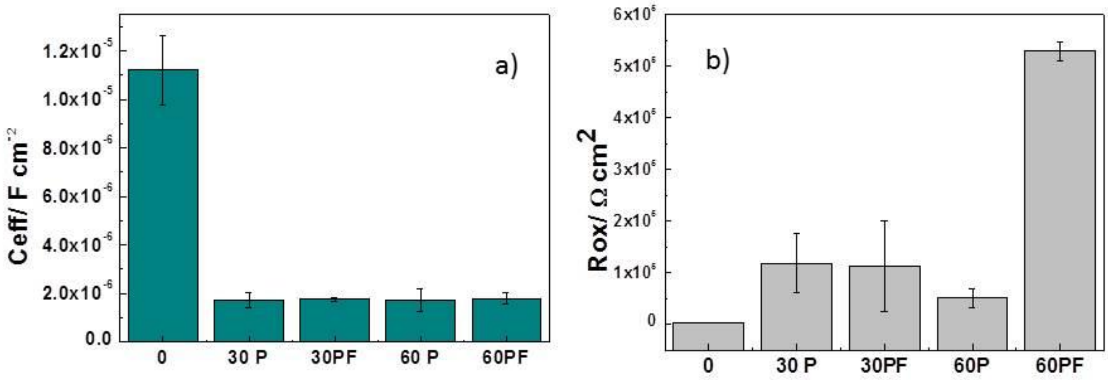

a)
Ceff/ F cm^-2
1.2x10^-5
1.0x10^-5
8.0x10^-6
6.0x10^-6
4.0x10^-6
2.0x10^-6
0.0
0
30 P
30PF
60 P
60PF
b)
Rox/ Ω cm2
6x10^6
5x10^6
4x10^6
3x10^6
2x10^6
1x10^6
0
0
30 P
30PF
60P
60PF

Figure 12

Figures legends.

Figure 1. Color samples after anodization process in phosphoric acid (left) and in phosphoric acid and sodium fluoride (right).

Figure 2. SEM micrographs for anodized zirconium samples 60P, 30P, 60PF and 30PF.

Figure 3. AFM measurements for anodized zirconium samples.

Figure 4. EDS spectra for anodized zirconium samples.

Figure 5. Raman spectra obtained for the as untreated zirconium and zirconium oxides anodized under different conditions.

Figure 6. XPS (a) Zr 3d and (b) O 1s spectra recorded at the surface of zirconium anodized in phosphoric acid at 30 V (30P) and 60 V (60P) and in phosphoric acid containing NaF at 30 V (30PF) and 60 V (60PF). Dashed lines denote the positions of reference spectra: a) Zr and ZrO_2, and b) O^{2-}, OH^- and H_2O/PO_4^{3-}.

Figure 7. XPS (a) P 2p and (b) F 1s spectra of zirconium anodized in phosphoric acid at 30 V (30P) and 60 V (60P) and in phosphoric acid + NaF at 30 V (30PF) and 60 V (60PF). Dashed lines denote the peak center.

Figure 8. XPS depth profiles of the layers formed by anodization of zirconium in (a) phosphoric acid at 60 V (60P) and (b) in phosphoric acid containing NaF at 60 V (60PF). Sputtering rate 0.67 nm/min is relative to the Ni/Cr standard.

Figure 9. Polarization curves for as-received zirconium (black line) and anodized zirconium samples; 30P (red line), 60P (green line), 30PF (blue line) and 60PF (pink line) recorded in Afnor artificial saliva.

Figure. 10. EIS diagrams for zirconium samples; as-received (■), 30P (◄), 60P (▲), 30PF (●) and 60PF (●) recorded in Afnor artificial saliva after 40 minutes stabilization at the open circuit potential.

Figure 11. Electrical equivalent circuit used for fitting EIS data.

Figure 12. Values of C_{eff} (a) and R_{ox} (b) obtained by fitting EIS data of anodized and as received zirconium samples in Afnor artificial saliva.

Table 1. Denotation of the zirconium samples according to the conditions of the anodization process.

Sample denotation	Anodization condition
60P	60 V in phosphoric acid (1mol/L)
30P	30 V in phosphoric acid (1mol/L)
60PF	60 V in phosphoric acid (1mol/L) + sodium fluoride (0.15% w/v)
30PF	30 V in phosphoric acid (1mol/L) + sodium fluoride (0.15% w/v)

Table 2. Chemical composition of artificial saliva Afnor

Compound	NaCl	KCl	Na_2HPO_4	$NaHCO_3$	KSCN	CH_4ON_2 (Urea)
Concentration (g/L)	0.7	1.2	0.26	1.5	0.33	1.3

Table 3. R_a values for the anodized zirconium samples.

Sample	R_a/ nm
30 P	381
60P	672
30PF	339
60PF	885

Table 4. Chemical composition of the layers formed by anodization of zirconium in phosphoric acid at 60 V (60P) or 30 V (30P) and in phosphoric acid containing NaF at 60 V (60PF) or 30 V (30PF). The composition was derived from XPS survey spectra after 4 minutes sputtering.

Element	Composition / atomic %			
	60P	30P	60PF	30PF
C	47.3	47.7	41.1	36.0
O	36.7	36.6	34.3	37.7
Zr	7.9	7.6	16.8	14.5
P	5.6	4.2	0.9	3.4
F	0	0	6.6	6.4
N	1.6	3.3	0	1.6
Na	0.8	0.6	0.2	0

Table 5. Electrochemical parameters* of anodized zirconium samples measured in Afnor artificial saliva.

Sample	**E_{corr} (V*vs* SCE)**	**$E_{breakdown}$ (V *vs* SCE)**	**j_{pass} (A/cm^2)**
60P	-0.47 ± 0.02	-0.89 ± 0.01	$7.45\cdot10^{-7}$± $1.2 \cdot10^{-7}$
30P	-0.45 ± 0.03	-0.95± 0.02	$4.75\cdot10^{-7}$± $0.6\cdot10^{-7}$
60PF	-0.38 ± 0.04	-0.48 ± 0.02	$3.47\cdot10^{-7}$ ±$1.2\cdot10^{-7}$
30PF	-0.62 ± 0.01	-0.64 ± 0.01	$4.92\cdot10^{-7}$ ± $1.7\cdot10^{-7}$

*E_{corr} corrosion potential, $E_{breakdown}$ breakdown potential, j_{pass} passivity current density

Highlights

Anodic oxide layer formed on Zr in phosphoric acid with fluoride is monoclinic ZrO2.

Fluorine ions from the electrolyte are incorporated in the oxide layer.

Anodic polarization in Afnor solution evidences breakdown of the passive films.

Decrease of breakdown potential may be induced by defects caused by fluorine